Chemical Engineering Journal 473 (2023) 145181

Contents lists available at ScienceDirect

Chemical Engineering Journal

journal homepage: www.elsevier.com/locate/cej

Turning the coordination environment of atomic Fe-N_4 center by peripheral nitrogen species for boosted catalytic performance

Fengliang Cao [a], Qingshan Zhao [a,*], Debin Kong [a], Xiaojie Tan [a], Xinxin Li [b], Tengfei Liu [a], Linjie Zhi [a,*], Mingbo Wu [a,*]

[a] State Key Laboratory of Heavy Oil Processing, College of Chemistry and Chemical Engineering, College of New Energy, China University of Petroleum (East China), Qingdao 266580, China

[b] Qingdao Key Laboratory of Functional Membrane Material and Membrane Technology, Qingdao Institute of Bioenergy and Bioprocess Technology, Chinese Academy of Sciences, Qingdao, 266101, China

ARTICLE INFO

Keywords:
Single-atom catalyst
Fe-N_4
Nitrogen dopant
Coordination environment regulation
Nitroarene reduction

ABSTRACT

Atomically dispersed metal-nitrogen-carbon (M-N-C) catalysts show great potential for heterogeneous catalysis. However, recognizing and engineering the microenvironment of M-N_x sites to achieve satisfactory catalytic performance remains challenging. Herein, we propose a facile g-C_3N_4-assisted template strategy to anchor atomic Fe-N_4 sites on highly nitrogen-doped carbon nanosheets. Through regulating the ratio and type of peripheral nitrogen species by carbonization temperature, the optimal Fe-N-C-800 catalyst showed significantly boosted catalytic activities (overall turnover frequency of 13.43 min^{-1} and activation energy of 19.44 kJ mol^{-1}) for nitroarene reduction with extremely low reductant dosage, exceeding most reported metal catalysts. Experimental and theoretical results reveal appropriate graphitic- and pyrrolic-N dopants surrounding the Fe-N_4 center can tailor the local electronic structure and contribute to obvious upshift of the d-band center, which dramatically promotes the adsorption and conversion of reactant substrates, eventually delivering the unprecedented catalytic performance. This work provides a guide for rational coordination environment regulation of single-atom catalysts for efficient chemical transformations.

1. Introduction

As one of the most promising research frontiers in catalysis, single-atom catalysts (SACs) have attracted intensive interest due to their compelling merits such as unique catalytic properties, ultrahigh atom efficiency, interesting structure–activity relationships, and so on [1–4]. The metal active sites form chemical bonds with elements on the supports thereby homogeneously monodispersed and anchored on the surface of the supports. This unique structural feature endows SACs with strong metal support interactions (SMSIs) [5–7] and customizable homogeneous active metal sites [8–10]. Therefore, SACs show promising potentials in the fields of energy storage [11,12], energy conversion [13–16], and chemical transformation [17–19] which are typically dominated by conventional metal catalysts.

Recently, nitrogen-coordinated atomically dispersed transition metals (e.g., Fe, Co, and Mn) anchored on carbon materials (M-N-C) have been preferred by researchers because of their cost-effectiveness and excellent stability [20–24]. As the vital fixed site, designing materials with high nitrogen loading has been an ideal approach to accommodate additional monoatomic with excellent catalytic activity [25]. For instance, Müllen et al., reported an *in-situ* trapping strategy to enhance the amount of accessible Fe-N_4 sites in the resulted Fe-N-C electrocatalysts by employing nitrogen-rich precursors such as melamine that can coordinate with Fe ions in zeolitic imidazolate frameworks to generate Fe-N_6, which transforms to atomically dispersed Fe-N_4 through a pyrolysis procedure [26]. However, in most cases, the exposed N atoms are prone to escape from the bulk material during the thermal treatment process, which results in low yield and inferior N content of the final product. This would lead to low single-metal atom loading, unsatisfactory catalytic activity, and harsh reaction conditions. Therefore, it is necessary to develop feasible strategies to efficiently capture nitrogen atoms for the synthesis of nitrogen-rich supports to enhance the accommodation of single metal atoms [27].

Additionally, recent studies have found that the local coordination environment shows a significant impact on the electronic properties and catalytic characteristics of the metal centers [9,28–32]. For example,

* Corresponding authors.
E-mail addresses: qszhao@upc.edu.cn (Q. Zhao), zhilj@upc.edu.cn (L. Zhi), wumb@upc.edu.cn (M. Wu).

https://doi.org/10.1016/j.cej.2023.145181
Received 22 May 2023; Received in revised form 18 July 2023; Accepted 31 July 2023
Available online 2 August 2023

Yuan et al., prepared an N/P dual-coordinated Fe single-atom catalyst, which is more favorable for the adsorption of oxygen intermediates for ORR in fuel cells [33]. Cao et al., reported an atomic Co_1/NPC catalyst with single Co_1-N_3P_1 sites that shows prominent catalytic activity and chemoselectivity for the hydrogenation of nitroarenes [34]. Still and all, most researchers exclusively paid attention to the coordination shell of metal centers. It is not rational to neglect the impact of various nitrogen configurations on the carbon matrix while considering the prospective excellence of metal-free N-doped carbon catalysts [35–37]. Therefore, elucidating the influence of peripheral nitrogen species on the micro-environment of M-N_x active sites is of great significance to modulate the catalytic performance of SACs.

Functionalized aromatic amines serve as crucial building blocks of fine chemicals, which have widespread applications in the production of pharmaceuticals, pigments, agrochemicals, and polymers [38]. Catalytic reduction of nitroarenes, an environmentally benign and recyclable approach for the synthesis of value-added amines, has attracted extensive attention. Although precious metal catalysts (e.g. Pd, Pt, Ru, etc.) have demonstrated excellent catalytic activities, the chemoselective reduction of the –NO_2 group without affecting other reducible bonds remains challenging [39]. Traditional non-precious metals (Fe, Co, Ni, etc.) and their sulfides have also been employed as alternative catalysts, which unfortunately suffer from lower catalytic activities [40]. Most recently, single-atom M-N-C catalysts show great potential for application in nitroarene reduction owing to their distinctive active site structure, which can simultaneously achieve high activity and selectivity [41]. Even so, there is still an urgent call for developing M-N-C catalysts with advanced catalytic performance and elucidating the intrinsic structure-performance relationship.

Herein, by employing petroleum asphalt as the carbon source and *in-situ* formed g-C_3N_4 nanosheets as the nitrogen source and template, atomic Fe-N_4 active sites with abundant peripheral nitrogen species were anchored on two-dimensional carbon nanosheets (Fe-N-C) for nitroarene reduction. The highly viscous asphalt could encapsulate the g-C_3N_4 nanosheets and accommodate the nitrogen source in the carbon skeleton to anchor the single metal atoms. More importantly, the peripheral nitrogen species can be tailored by the carbonization temperature, which efficiently modulate the local coordination environment of the Fe centers. Benefiting from the rich outer-shell nitrogen species surrounding the Fe-N_4 center, as well as the porous nanosheet structure, the optimized Fe-N-C-800 catalyst exhibited distinguished catalytic activities for the selective reduction of nitroarenes to corresponding amines at low reductant dosages, superior to most reported precious and non-precious metal catalysts.

2. Experimental

2.1. Materials and chemicals

Petroleum asphalt was obtained from China National Offshore Oil Corporation (19.63 wt% saturates, 30.13 wt% aromatics, 37.21 wt% resins, and 7.40 wt% asphaltenes). Dicyandiamide (98 wt%), HCl (37 wt %), $FeCl_3$(99 wt%), ethanol (99 wt%), $NaBH_4$ (98 wt%), KSCN (99 wt%), 4-nitrophenol (4-NP, 99 wt%), nitrobenzene (99 wt%), 4-nitrochlorobenzene (99 wt%), 4-nitrobromobenzene (99 wt%), 4-nitrotoluene (99 wt%), 4-nitrobenzonitrile (99 wt%), 4-nitrobenzyl alcohol (99 wt%), 4-nitrobenzaldehyde (99 wt%), and 4-nitroanisole (99 wt%) were purchased from Aladdin Industrial Corporation. All the chemical reagents were used as received without further purification.

2.2. Synthesis of Fe-N-C samples

Petroleum asphalt (0.25 g) was homogeneously dissolved in 30 mL of toluene with the assistance of ultrasonication. Then, 1 g of dicyandiamide (DICY) was added into the solution with intense stirring to form a uniform suspension. The mixture was dried under reduced pressure to obtain a gray power, which was carbonized at 550 °C for 4 h with a heating rate of 2.3 °C min^{-1} under N_2 atmosphere, obtaining a sandwich-like g-C_3N_4 and carbon (SGC) intermediate. 0.5 g of SGC and 0.05 g of $FeCl_3$ were mixed and dispersed in 20 mL of acetone with vigorous stirring. The mixture was dried at 60 °C to remove the solvent and carbonized at different temperatures (700, 800, 900, and 1000 °C) for 2 h with a heating rate of 2 °C min^{-1} under N_2 atmosphere. The power was etched with 1 M HCl solution and thoroughly washed with distilled water, labeled as Fe-N-C-T (T=700, 800, 900, and 1000), respectively. Taken as controls, petroleum asphalt-derived carbon (PAC) samples were directly prepared by calcining petroleum asphalt at 550 °C (PAC-550) and 800 °C (PAC-800) under N_2 atmosphere without adding DICY and $FeCl_3$. Fe-C-800 and N-CNS were synthesized with the same method as Fe-N-C-800 except for the addition of DICY and $FeCl_3$, respectively.

2.3. Characterization

Thermogravimetric analysis (TGA, TGA4000, PerkinElmer) was carried out under N_2 atmosphere from 50 °C to 1000 °C with a heating rate of 10 °C min^{-1}. The crystal structure of the samples was characterized by X-ray diffraction (XRD, X'Pert PRO MPD) using Cu Kα radiation (k = 1.518 Å). The chemical structure was investigated by Fourier-transform infrared spectroscopy (FTIR, Thermo NEXUS 470). Scanning electron microscopy (SEM, Hitachi S-4800) and transmission electron microscopy (TEM) images (JEM-2100F) were used to investigate the structure and morphology. High-angle annular dark-field scanning transmission electron microscopy (HAADF-STEM) images were carried out on a spherical aberration-corrected Titan 80–300 operated at 300 kV. The elemental composition and chemical bonding were studied by XPS with Mg K_α radiation (1486.6 eV) monochromatic X-ray source (Thermo Scientific Escalab 250XI). The content of iron was detected by inductively coupled plasma optical emission spectroscopy (ICP-OES, Vista-MPX). X-ray absorption near edge structure (XANES) and extended X-ray absorption fine structure (EXAFS) were performed at 1W1B station in Beijing Synchrotron Radiation Facility (BSRF) to reveal the coordination structure. The catalytic activity of the catalysts was monitored by a UV–vis spectrophotometer (Shimadzu, UV-2700).

2.4. Catalytic nitroarene reduction

In a typical procedure, 2.0 mg catalyst was dispersed into 20 mL water/ethanol (v/v=1:1) solution containing the nitroarene substrate (5 mM), which was then immersed in a water bath (30 °C). 12.5 equivalent of $NaBH_4$ was added into the dispersion with vigorous stirring. The reduction of nitroarene was monitored by UV–vis UV–Vis spectroscopy. To reveal the thermodynamics and reaction kinetics, catalytic reduction of nitroarene over Fe-N-C-800 was conducted at temperatures of 30–90 °C and different reactant usages (12.5–50 equivalent). For the recycling test, the catalyst was separated from the suspension via centrifugation and washed with distilled water for three times. After drying at 60 °C, the catalyst was reused in subsequent reaction cycles. Repeated experiments were carried out for averaging catalytic data. Overall turnover frequency (TOF) of the catalysts was calculated as: TOF (min^{-1}) = [mol of substrate reduced] / [mol of metallic Fe * reaction time (min)].

2.5. Adsorption experiment

The adsorption amount of 4-NP on various Fe-N-C-T catalysts was measured by adding the sample (10 mg) into 10 mL water/ethanol (v/v=1:1) solution containing 20 μmol of 4-NP. The suspension was stirred continuously at room temperature for 4 h and then left to stand for 8 h. The sample was filtered to remove the solid, and the concentration of residual 4-NP was measured by a UV–vis spectrophotometer. The adsorption capacity can be calculated as: Adsorption capacity = [Total

amount of 4-NP - residual amount of 4-NP (μmol)] / [catalyst weight (g)].

2.6. Density functional theory (DFT) calculations

All DFT calculations were performed using Ab-initio Simulation Package (VASP). All electron exchange–correlation functionals were calculated using the generalized gradient approximation (GCA) with the revised Perdew-Burke-Ernzerhof (PBE) method using a cutoff energy of 500 eV. Based on the lattice size, the Monkhorst-Pack meshes of 3×3×1 k-point samplings in the surface Brillouin zones were used for the graphene surfaces with a unit cell of 5×5×1. A vacuum layer exceeding 15 Å was used to avoid periodic interactions. The atomic position was fully relaxed until the maximum force on each atom was less than −0.01 eV/Å and 10^{-5} eV. The selection of these parameters was based on convergence tests with respect to the total energy of the systems.

3. Results and discussion

3.1. Catalyst synthesis and characterization

The atomically dispersed Fe-N-C catalysts with abundant nitrogen dopant were synthesized through a facile sacrificial template strategy as illustrated in Fig. 1a. As a byproduct in petroleum refining, petroleum pitch is rich in asphaltenes and aromatic compounds, which provides as a versatile carbon precursor for the construction of carbon-based materials with regulable morphologies. A mixture of petroleum pitch and DICY was calcined at 550 °C to yield two-dimensional g-C_3N_4 templates, which was wrapped by the highly viscous petroleum asphalt to construct a sandwich-like g-C_3N_4 and carbon (SGC) composite. Subsequently, the iron source ($FeCl_3$) was immersed into the interbedded SGC, followed by a secondary carbonization procedure. TGA of DICY reveals complete decomposition of the lamellar g-C_3N_4 template after 740 °C, during which process the released gas would adequately dope the matrix to achieve highly nitrogen-doped carbon nanosheets (Figure S1). As shown in Figure S2a, SGC shows similar FTIR spectrum to that of g-C_3N_4, which presents the characteristic s-triazine ring vibration at around 810 cm^{-1}, combined with CN heterocyclic stretching vibrations at 1260, 1339, 1420, 1575, and 1630 cm^{-1}. In the meanwhile, diffraction peaks of g-C_3N_4 at 13.1° and 27.4° can also be observed in the XRD pattern of SGC (Figure S2b), which is absent in the XRD spectrum of PAC-550, confirming the *in-situ* formation of g-C_3N_4 template [42]. After the secondary carbonization treatment, all characteristic peaks of g-C_3N_4 disappear in the FTIR spectra and XRD patterns of N-CNS-800 and Fe-N-C-800, suggesting that g-C_3N_4 was thoroughly decomposed to obtain N-doped and Fe, N-codoped carbon materials. Consequently, diffraction peaks at 26° and 43° corresponding to amorphous graphite can be observed in the XRD patterns of N-CNS-800 and Fe-N-C-800 [43]. Moreover, XRD pattern of Fe-C-800 shows characteristic diffraction peaks of Fe_3C crystals. This result reveals the significant role of the abundant nitrogen dopants, which provide reinforced tongs to disperse the metal atoms to generate atomic Fe-N_x sites.

SEM and TEM images were carried out to investigate the structure and morphology of the samples. As shown in Figure S3, compared with the bulk morphology of petroleum asphalt-derived carbon samples (PAC-550 and PAC-800), SEM image of SGC intermediate shows a layer-

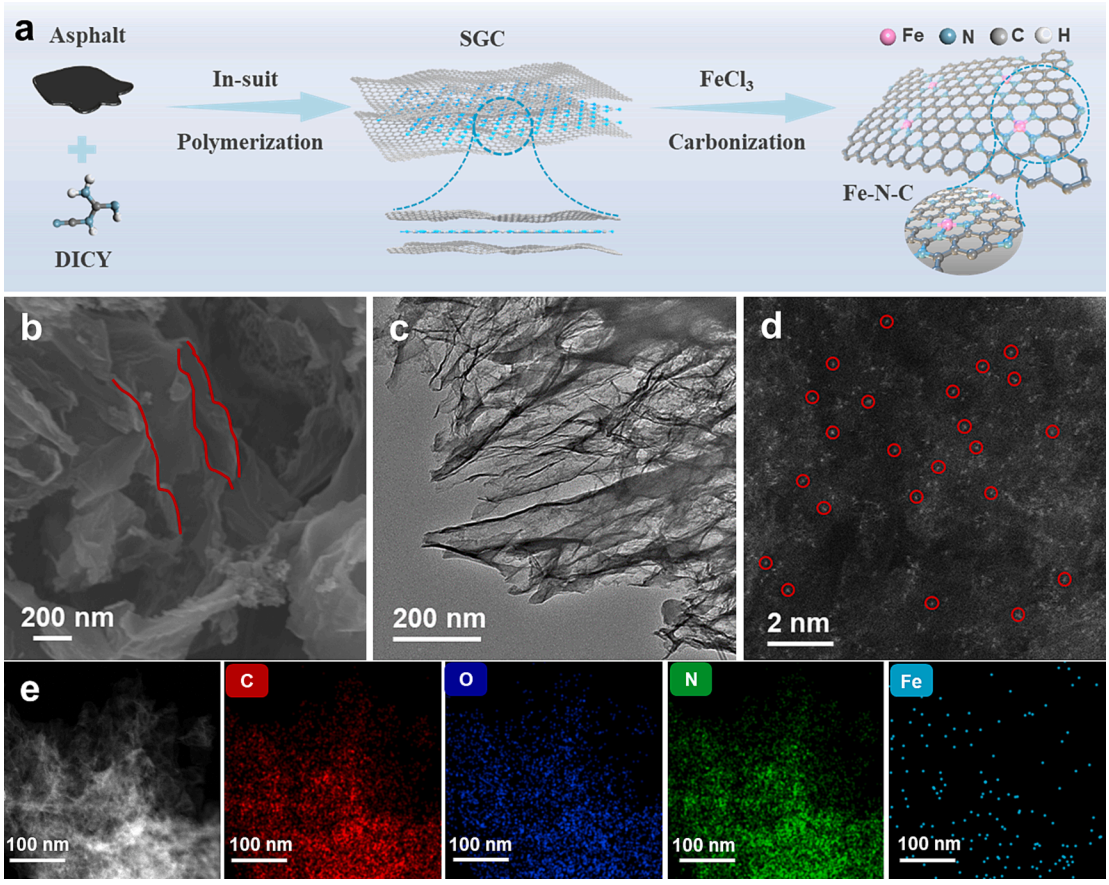

Fig. 1. Synthetic strategy and morphological characterizations. a) Schematic illustration of the preparation strategy for Fe-N-C. b) SEM image and c) TEM image of Fe-N-C-800. d) AC-HAADF STEM image of Fe-N-C-800; the Fe atoms are marked with red circles. e) TEM image and corresponding EDS mapping of Fe-N-C-800 showing the dispersion of C (red), N (green), O (dark blue), and Fe (light blue). (For interpretation of the references to color in this figure legend, the reader is referred to the web version of this article.)

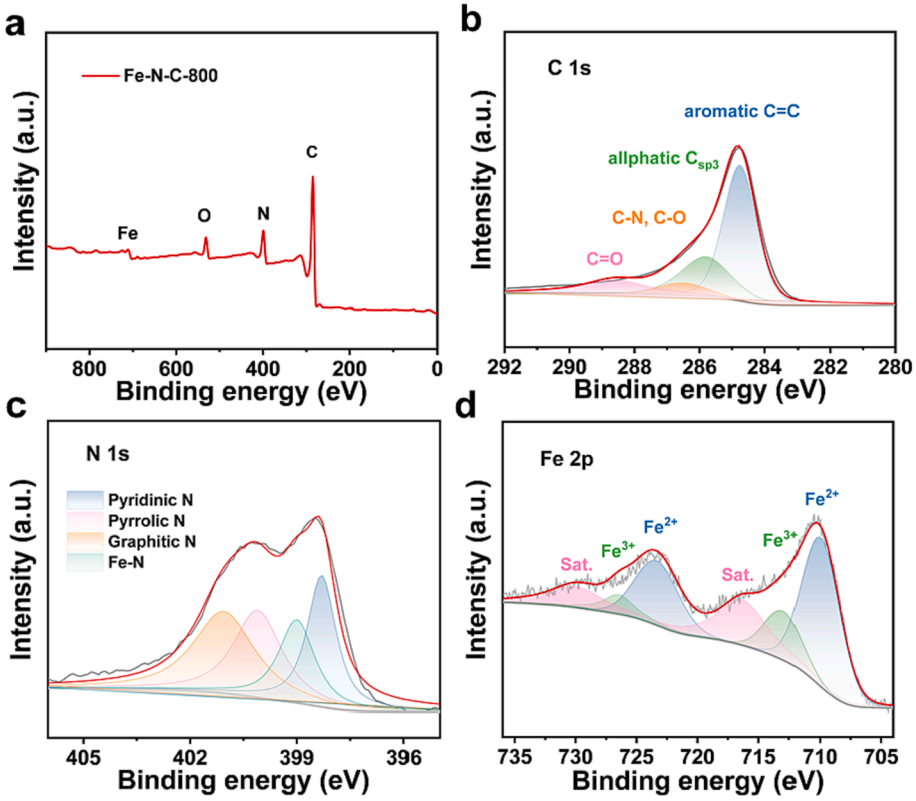

Fig. 2. a) XPS survey spectrum, b) C 1 s XPS spectrum, c) N 1 s XPS spectrum, and d) Fe 2p XPS spectrum of Fe-N-C-800.

by-layer sandwich-like structure, which is composed of carbon and nitrogen elements (Figure S4). SEM and TEM images of N-C-800 and Fe-N-C-800 demonstrate their ultrathin two-dimensional morphology, indicating the efficient structure-directing role of the lamellar g-C_3N_4 template (Fig. 1b-c). No Fe crystals or particles can be found in the Fe-N-C-800 sample. Thus, aberration-corrected HAADF-STEM was employed to further elucidate the existence of Fe species. As shown in Fig. 1d, isolated bright spots marked with red circles can be clearly observed on the carbon nanosheet substrate, indicating the formation of the atomically dispersed Fe atoms. Corresponding elements mapping images further display the uniform distribution of C, O, N, and Fe on the whole carbon skeleton of Fe-N-C-800 (Fig. 1e). N_2 adsorption–desorption analysis reveals the porous structure of the samples (Figure S5). Compared with PAC-800, the increased specific surface area and pore volume of SGC should be ascribed to released gas during the formation of g-C_3N_4. After complete decomposition of g-C_3N_4 through secondary carbonization, the Fe-N-C-T samples show increased specific surface areas with plenty of micropores. Such porous nanosheet structure would efficiently facilitate the exposure of Fe-N_x active sites and accelerate mass transfer in the reaction processes [44]. Notably, with the increasing of calcination temperature, the surface area and pore volume of Fe-N-C-T show a first rise then descend tendency, which should be attributed to the pore-forming effect of pyrolysis gas and gradual graphitization of the carbon skeleton (Table S1). This is verified by the Raman results, as the I_D/I_G value of Fe-N-C-T samples gradually decreases with the increasing of calcination temperature (Figure S6).

The chemical states of different elements in Fe-N-C-800 were further examined by XPS. XPS survey spectrum of Fe-N-C-800 clearly shows the appearance of C, N, O, and Fe signals (Fig. 2a). The high-resolution C 1 s spectrum (Fig. 2b) is composed of four peaks, including C=C (284.8 eV), aliphatic C_{sp3} (285.8 eV), C=N/O (286.0 eV), and O-C=O (288.5 eV) [31]. The high-resolution N 1 s spectrum of Fe-N-C-800 can be deconvoluted into four peaks (Fig. 2c), which are assigned to pyridinic N (398.4 eV), Fe-N moiety (399.0 eV), pyrrolic N (399.9 eV), and graphitic N (401.1 eV), respectively. The two peaks in the Fe 2p spectrum indicate that the valence state of Fe atom is between +2 and +3 (Fig. 2d) [45]. Remarkably, as a result of sufficient nitrogen provided by the g-C_3N_4 template, the nitrogen content in Fe-N-C-800 is determined to be 10.32 at.% (Table S2), which is much higher than most reported single-atom M-N-C catalysts [46]. Such abundant nitrogen dopants can not only stabilize the atomically dispersed Fe species, but also modulate the atom arrangement on the substrate to tailor the local coordination environment of metal centers. According to the ICP-OES test listed in Table S2, the metal loading in Fe-N-C-800 was determined to be 2.97 wt.%.

X-ray absorption fine structure (XAFS) analysis was carried out to unravel the valance states and detailed structural information of the Fe-N-C-800 catalyst. According to the XANES analysis (Fig. 3a-b), the rising edge for Fe in Fe-N-C-800 is between iron phthalocyanine (FePC) and Fe_2O_3, suggesting the valence of Fe atoms is between +2 and +3 [26], which is well accordance with the XPS result. The oxidation state of Fe atoms, which is obtained by the first inflection point of the derivative spectrum, is linearly dependent on the position of the absorption edge. Accordingly, the Fe K-edge linear fitting curve reveals that the Fe species in Fe-N-C-800 has a higher oxidation state (+2.7) than that of FePC (+2) (Fig. 3c), which should be attributed to the stronger electron transfer from Fe to coordinated N atoms induced by peripheral nitrogen species on the support [47]. The k^3-weighted Fourier-transform Fe K-edge (FT-EXAFS) spectrum of Fe-N-C-800 (Fig. 3d) shows a prominent peak at 1.52 Å that is nearly identical to FePC, indicating the presence of Fe-N scattering path [48]. The Fe-Fe peak at 2.21 Å is neglectable, further excluding the presence of Fe clusters or particles in Fe-N-C-800. Due to the powerful resolutions in both k and R spaces, wavelet transformed of Fe K-edge EXAFS (WT-EXAFS) was conducted to carefully examine the dispersion of Fe (Fig. 3g). In contrast to the WT plots of Fe foil, Fe_2O_3, and FePC, the WT contour plots of Fe-N-C-800 show only one intensity maximum at 5 $Å^{-1}$ assigned to the Fe-N bond [49], with no intensity maximum corresponding to Fe-Fe. Further quantitative EXAFS curve fitting analysis shows that the coordination number of Fe atoms is 4.3

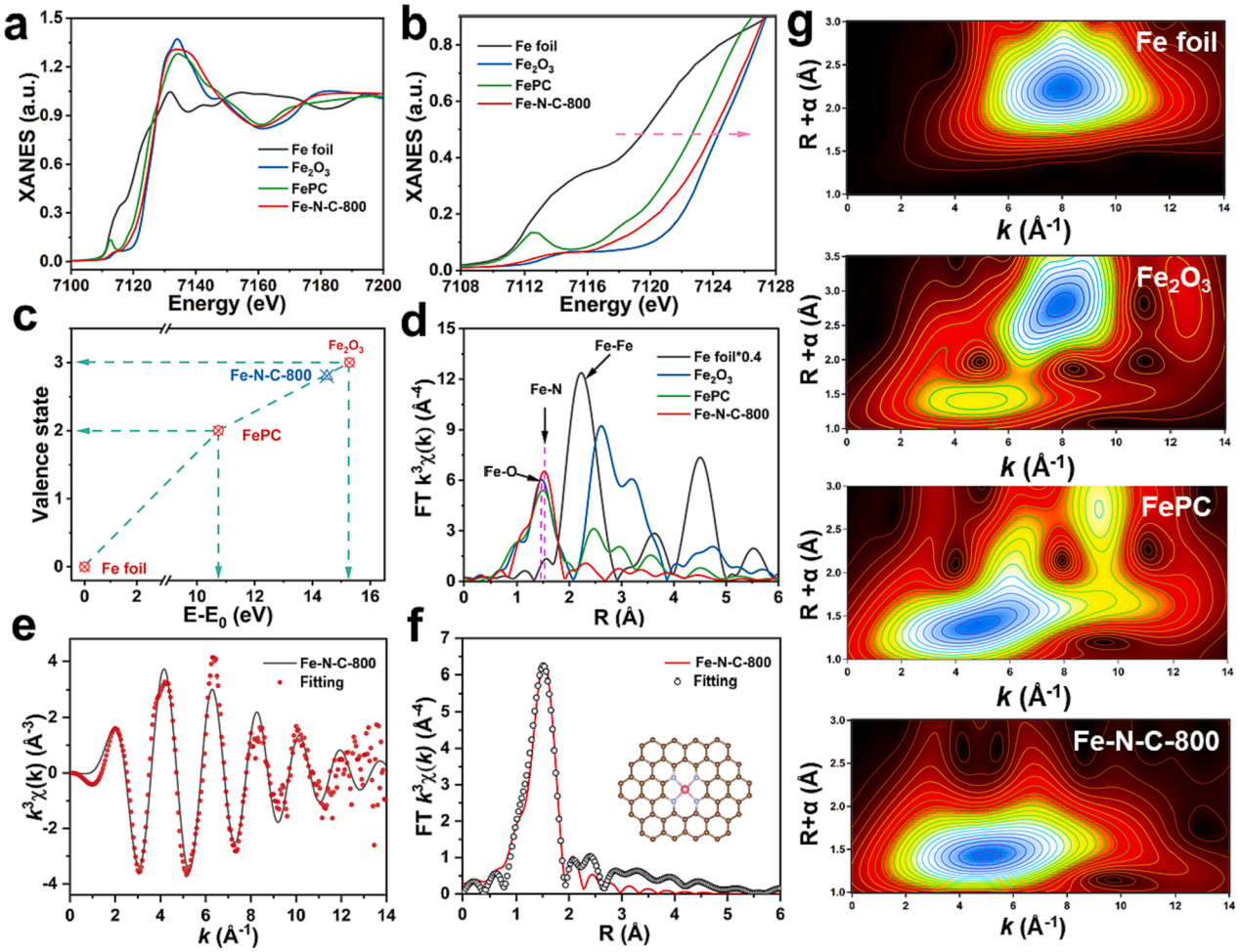

Fig. 3. Coordination and electronic states of Fe-N-C-800. a) Fe-K edge XANES spectra of Fe-N-C-800 and reference samples. b) A magnified image of the absorption edge region. c) Fe K-edge linear fitting curve of Fe-N-C-800, Fe foil, FePC, and Fe_2O_3. d) FT-EXAFS spectra of Fe-N-C-800, Fe foil, FePC, and Fe_2O_3. e) The fitting of the FT-EXAFS spectrum of Fe-N-C-800 in the k space. f) The fitting of the FT-EXAFS spectrum of Fe-N-C-800 in the R space; the inset is the schematic model of Fe-N_4 center. g) WT Fe K-edge EXAFS profiles of Fe foil, Fe_2O_3, FePC, and Fe-N-C-800.

with an average bond length of 2.02 Å, suggesting that the Fe atoms are predominantly coordinated with four pyridinic N atoms to generate a Fe-N_4 configuration (Table S3 and Fig. 3f, inset). For comparison, the fitting results of Fe foil, Fe_2O_3, and FePC are displayed in Figure S7-S9, respectively. Moreover, XAFS results demonstrate Fe atoms are atomically dispersed and coordinated with N atoms to achieve atomic Fe-N_4 configurations for Fe-N-C-T (T=700, 800, 900) samples except for Fe-N-C-1000 (Figure S10 and Table S3). This should be attributed to the significant reduction of nitrogen species at 1000 °C, which are unable to stabilize the Fe atoms and results in the formation of Fe_3C crystals (Figure S11).

3.2. Catalytic reduction of nitroarenes

To evaluate the catalytic performance of the prepared catalysts, catalytic reduction of 4-nitrophenol (4-NP) to 4-aminophenol (4-AP) was chosen as a model reaction by employing $NaBH_4$ as the reductant. The reduction process was monitored by a UV–vis spectroscopy. The 4-NP solution exhibited a strong absorption peak at 317 nm, which offset to 400 nm after adding $NaBH_4$ along with a color change from light yellow to bright yellow [50] (Fig. 4a). After adding the Fe-N-C-800 catalyst, the absorption peak at 400 nm rapidly dropped, along with a concomitant emerging peak at about 300 nm, suggesting the smooth conversion of 4-NP to 4-AP (Fig. 4b). No peak could be found at 302 or 388 nm corresponding to 4-benzoquninoe monoxime or 4-nitrosophenol byproducts. As shown in Fig. 4c, the reaction could hardly proceed in the presence of reducing agent without any catalyst. The SGC intermediate is not an effective catalyst and gave an extremely low conversion (<10%). A 32% conversion was obtained over N-CNS-800 within 20 min, indicating that the abundant nitrogen species on carbon could provide metal-free catalytic active sites [51]. Further introduction of Fe single atoms induced a massive rise in the catalytic efficiency, which achieved a 100% conversion within 7 min for Fe-N-C-800. By contrast, Fe-C-800 showed a poor catalytic activity with a conversion of 6%, which further confirms the significant role of nitrogen dopants. Notably, it took 21 mins to completely convert the substrate for commercial Pd/C catalyst with the same amount of active sites, demonstrating the superior catalytic activity of Fe-N-C-800. Moreover, the Fe-N-C-800 catalyst showed excellent reusability and could be recycled for five cycles without any activity deterioration (Fig. 4d). The remarkable stability of Fe-N-C-800 was further verified by hot-filtration experiment. After filtrating out Fe-N-C-800 from the mixture system at 2 min, the reaction didn't proceed anymore under identical conditions, implying no leaching of Fe active species (Fig. 4e). To identify the intrinsic active sites of the Fe-N-C-800 catalyst, thiocyanate ion (SCN^-) poisoning experiment was carried out as atomic Fe-N_x moieties can be poisoned and deactivated by coordinating with SCN^- [52,53]. After being treated with KSCN for 24 h, the catalytic activity of Fe-N-C-800 showed a dramatic deterioration from 100% to 30%. The residual activity is comparable to that of N-CNS-800, arising from the catalytic effect of metal-free nitrogen-

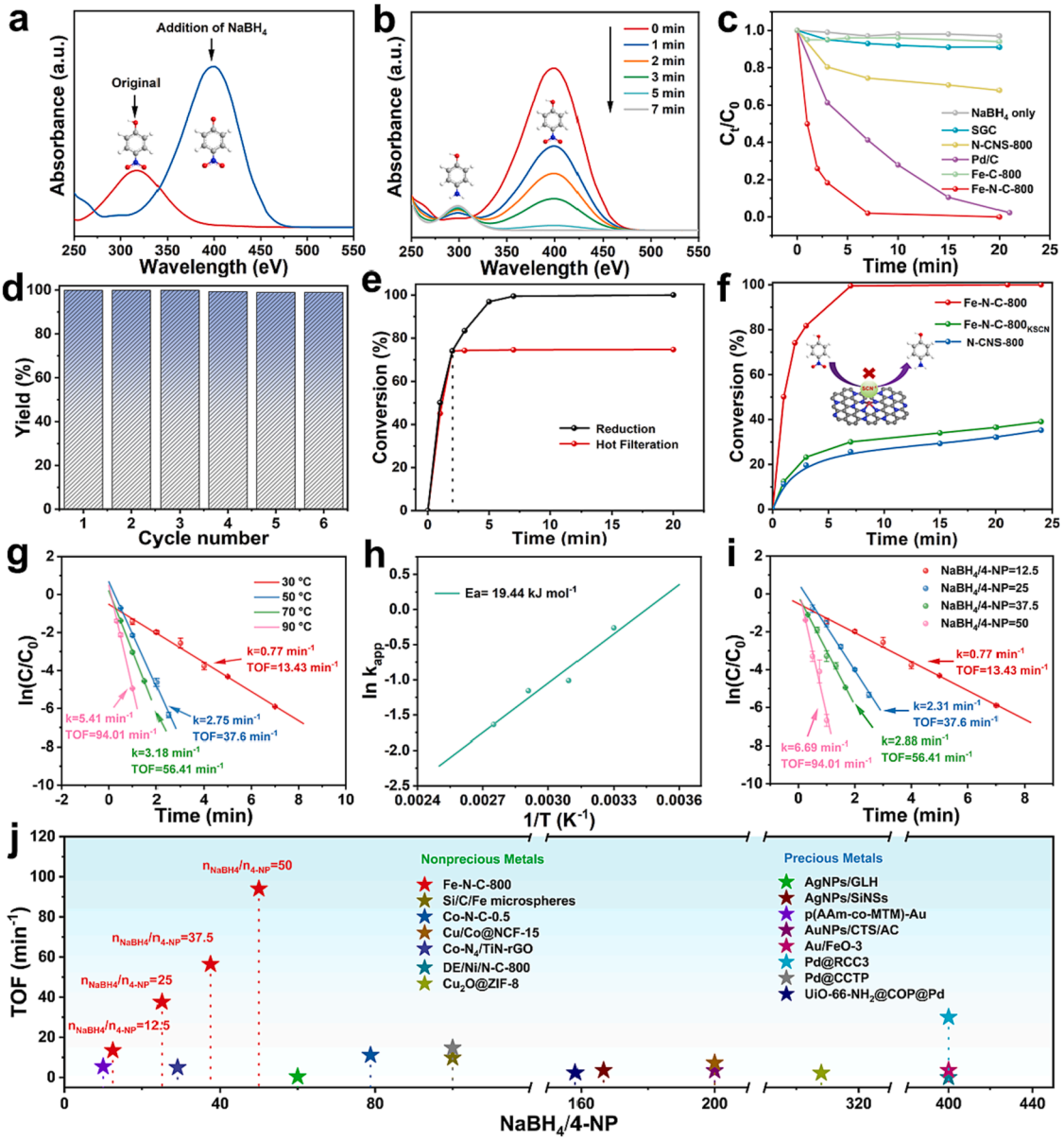

Fig. 4. Catalytic performance of Fe-N-C-800 for the reduction of 4-NP. a) UV absorption before and after the addition of $NaBH_4$. b) UV–vis absorption spectra of 4-NP catalyzed by Fe-N-C-800 at a certain time interval. c) Performance evaluation of various catalysts. d) The recycling test of Fe-N-C-800. e) Hot-filtration test of Fe-N-C-800. (f) Poisoning test of Fe-N-C-800. h) The relationships between $\ln(c_0/c)$ and reaction time at different reaction temperatures and g) corresponding Arrhenius plots for Fe-N-C-800. i) Influence of reductant dosage ($n_{NaBH4}/n_{4\text{-}NP}$) on the catalytic activity. j) Comparison of the catalytic activities with reported catalysts. Standard reaction condition: 20 mL 4-NP (5 mM), 12.5 equivalent $NaBH_4$, 2 mg catalyst, 30 °C.

doped carbon (Fig. 4f) [51]. Therefore, the atomically dispersed Fe-N_4 sites contributes to dominating catalytic efficiency for the reduction of 4-NP.

The catalytic reduction of 4-NP over metal-based catalysts follows pseudo-first-order kinetics [50], and the rate constant (k_{app}) value can be estimated by the linear relationship between $\ln(C_t/C_0)$ and the reaction time t. Considering the important metric of activation energy (E_a) for assessing the catalytic efficiency, the k_{app} and corresponding overall turnover frequency (TOF) values for 4-NP reduction at various temperatures were tested (Fig. 4g). The reaction kinetics improved significantly with the increase of reaction temperature. When the temperature reached 90 °C, the Fe-N-C-800 catalyst delivered a k_{app} and TOF of 5.41 and 94.01 min^{-1}, respectively. According to the Arrhenius plot of Ln k vs 1/T shown in Fig. 4h, the E_a value was calculated to be 19.44 kJ mol^{-1}, which is substantially lower than most reported catalysts (~ 30 kJ mol^{-1}) [54,55]. Especially, greatly excessive reactant with mole ratio of $NaBH_4$ to 4-NP ($n_{NaBH4}/n_{4\text{-}NP}$) ranging from 100 to 1000 was needed for general catalytic systems. To reveal the outstanding performance of Fe-N-C-800, the effect of $NaBH_4$ dosage on the catalytic efficiency was evaluated, as shown in Fig. 4i. Interestingly, the reaction could smoothly proceed with a high concentration of 4-NP (5 mM) and rather low $n_{NaBH4}/n_{4\text{-}NP}$ of 12.5, achieving a k_{app} and TOF of 0.77 and 13.43 min^{-1}, respectively. When the ratio of $NaBH_4$ to 4-NP was increased to 50, the k_{app} and TOF considerably rose to 6.69 and 94.01 min^{-1}, respectively, which stands out compared with precious- and nonprecious- metal catalysts (Fig. 4j and Table S4). Moreover, the Fe-N-C-800 catalyst also exhibited excellent catalytic activities toward the reduction of a series of nitroarenes to corresponding aromatic amines (Table S7), demonstrating its unprecedented catalytic performance and great potential for practical applications.

Due to the high nitrogen content, two-dimensional structure, and complete decomposition at high temperatures (>740 °C), g-C_3N_4 is

employed as sacrificial template for the synthesis of nitrogen-rich carbon matrix [42]. Importantly, it is found that the content and type of nitrogen species can be tailored by adjusting the carbonization temperature. XPS spectra of Fe-N-C-T samples show that full width at half maximum (FWHM) of the aromatic C-C peak narrows with the increasing of carbonization temperature, implying increased graphitization extent (Figure S12 and Table S5). Especially, the pyridinic N peaks in Fe-N-C-T show negative shifts of 0.2 eV compared with N-CNS-800, suggesting that the pyridinic N atoms coordinate with Fe to form pyridine-type Fe-N_4 centers (Fig. 5a). Due to the thermal instability of pyridinic- and pyrrolic-N, they tend to decompose or reorganize with surrounding carbon to form graphite-type N at high temperatures. In consequence, the percentage of pyridinic and pyrrolic N peaks decreases with the increasing of temperature, while graphitic N maintains almost unchanged due to higher structural stability (Fig. 5b). Quantitative analysis of the nitrogen species reveals the value of $n_{Pyridinic\ N}/n_{Fe}$ remains around 4.0 for Fe-N-C-800 and Fe-N-C-900 (Table S5), suggesting that most pyridinic N atoms coordinate with Fe to form the Fe-N_4 configurations. So it is reasonable that pyrrolic- and graphitic-N are the peripheral nitrogen species surrounding the coordination shell of Fe-N_4. According to the values of $n_{Pyrrolic\ N}/n_{Fe}$ and $n_{Graphitic\ N}/n_{Fe}$, the pyrrolic N outside the first-shell layer of Fe-N_x significantly decreases, while the percentage of outer-shell graphitic N shows a rising trend. The different coordination environments of Fe-N-C-T show a crucial impact on their catalytic performance, as shown in Fig. 5c and Table S6. Although Fe-N-C-700 has the highest nitrogen content, the catalyst only gave an inferior catalytic activity (TOF=1.93 min^{-1}), which should be attributed to incomplete pyrolysis of g-C_3N_4 template. With the efficient atomic Fe-N_4 active sites assisted by abundant peripheral pyrrolic- and graphitic-N dopants, Fe-N-C-800 exhibited a prominent catalytic efficiency. Further increasing of calcination temperature results in gradual decline for the catalytic performance of Fe-N-C-900 and Fe-N-C-1000, delivering a TOF of 8.71 and 5.32 min^{-1}, respectively. Considering the addition of excess $NaBH_4$, the catalytic activity apparently depends on the adsorption of reactants. To shed light on this, adsorption experiments of 4-NP were measured (Fig. 5d). Obviously, Fe-N-C-800 exhibited the maximum 4-NP adsorption capacity, which is supported by the color change of 4-NP solutions (Figure S13). Therefore, the promoted adsorption ability, which should be induced by the optimal pyrrolic- and graphitic-N surrounding the pyridine-type Fe-N_4 centers, contributes to the superior catalytic performance of Fe-N-C-800.

3.3. Theoretical calculations

The possible reaction route for the reduction of 4-NP over the Fe-N-C catalysts is proposed and shown in Fig. 6a. To begin with, BH_4^- reacts with Fe single atoms to form Fe-H intermediates via breakdown the B-H bond. Subsequently, the $H^\cdot$ radical adducts of Fe-H intermediates would attack the nitrogen in the $-NO_2$ of 4-NP, which is transformed into 4-AP after the hydrogenation process. Finally, 4-AP is desorbed from the catalyst surface and creates a free surface for the next reaction cycle [56,57]. To shed light on the influence of coordination environment on

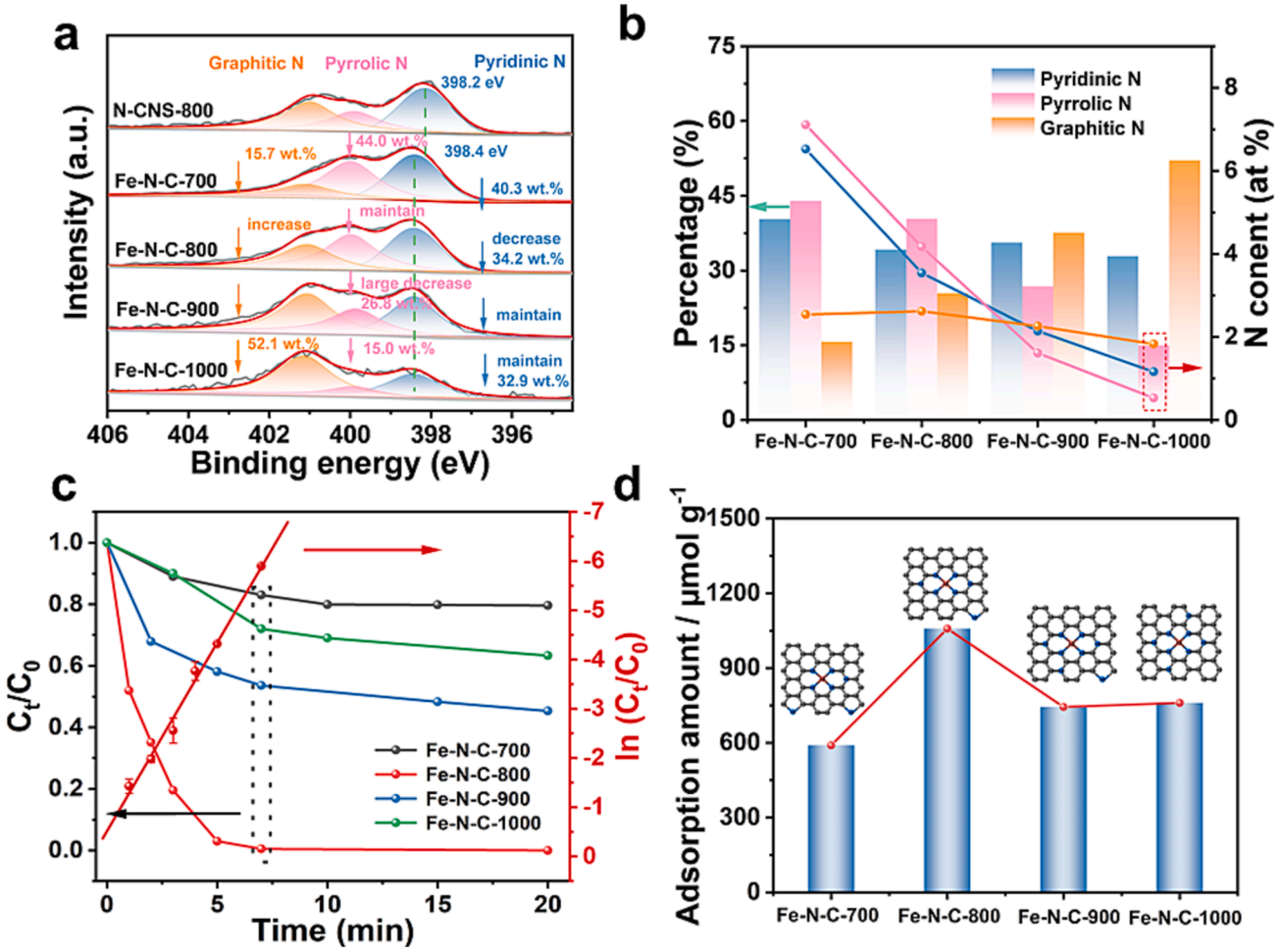

Fig. 5. Characterization and catalytic performance of Fe-N-C-T. a) High-resolution N 1 s XPS spectra of Fe-N-C-T. b) Proportion of pyridinic N, pyrrolic N, and graphitic N species in Fe-N-C-T. c) Catalytic reduction of 4-NP over Fe-N-C-T and Pseudo-first-order plot of ln(c/c_0) against reaction time for Fe-N-C-800. d) Adsorption amounts of 4-NP on Fe-N-C-T.

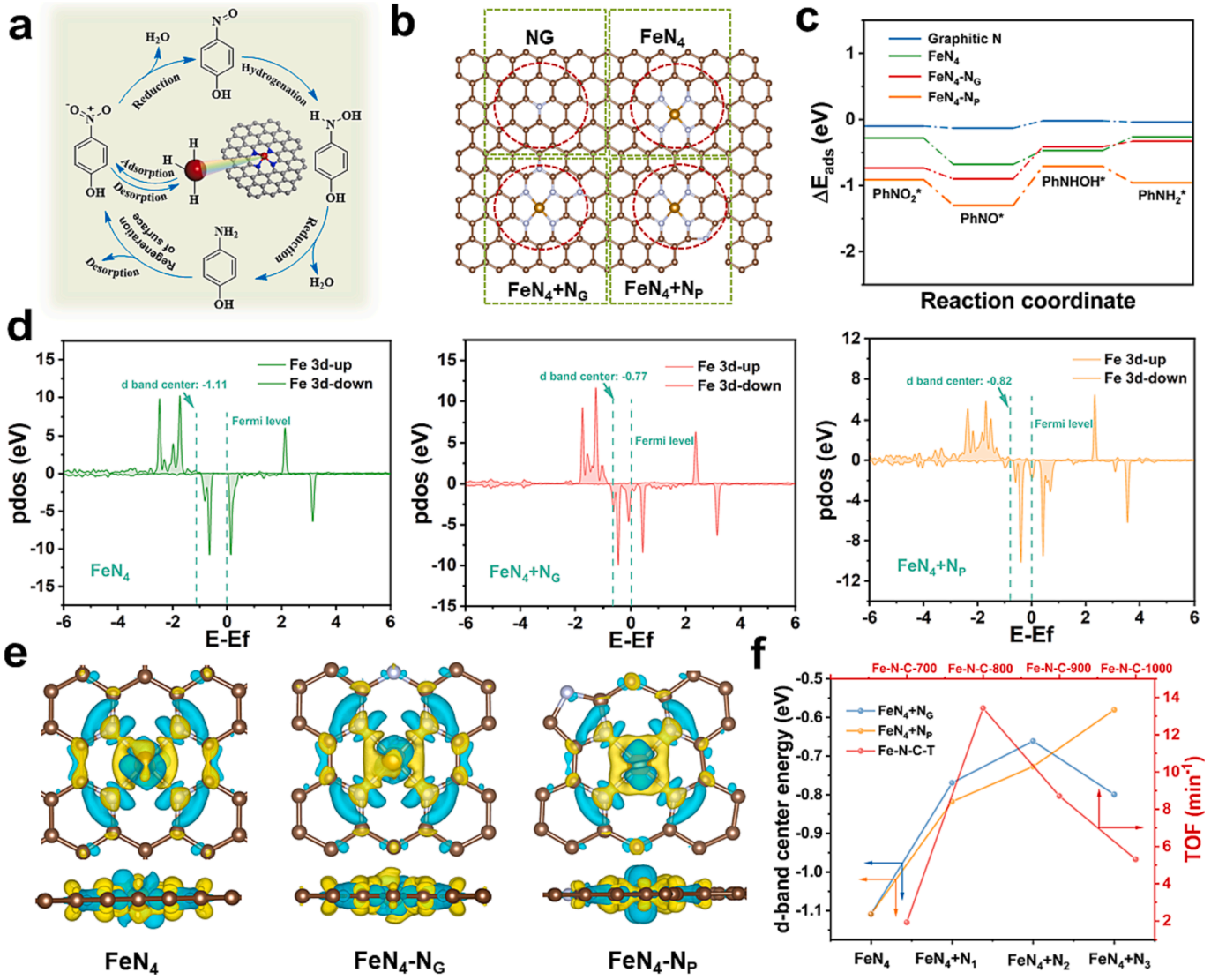

Fig. 6. Theoretical analysis of the active center structure and catalytic performance. a) Schematic diagram of the reaction pathway for the reduction of 4-NP to 4-AP. b) Optimized structures of four models: graphitic N, FeN_4, FeN_4-N_G, and FeN_4-N_P. c) Potential energy profiles of 4-NP reduction on four models. d) DOS of Fe-N_4, FeN_4-N_G, and FeN_4-N_P. e) Charge density difference of FeN_4, FeN_4-N_G, and FeN_4-N_P. Yellow and blue represent electron gain and loss, respectively. f) The relationship between the d-band center of different models and TOF of Fe-N-C-T. (For interpretation of the references to color in this figure legend, the reader is referred to the web version of this article.)

the catalytic performance, DFT calculations were conducted to elucidate the role of peripheral N species. Based on the XPS and XAFS analysis results, four configurations of graphitic N, FeN_4, FeN_4-graphitic N (FeN_4+N_G), and FeN_4-pyrrolic N (FeN_4+N_P) were constructed, as illustrated in Fig. 6b. According to the reaction mechanism, the adsorption energies of reactant, intermediates, and product on the surface of the four models were calculated (Fig. 6c). The adsorption energies of 4-NP, 4-nitrosophenol, 4-hydroxy-hydroxylaniline, and 4-AP on the graphitic N model are calculated to be -0.10, -0.12, -0.02 and -0.04 eV, respectively, revealing spontaneous proceeding of the reduction process over the metal-free catalyst. The absorption energy barrier of 4-NP becomes lower over FeN_4, suggesting that FeN_4 can rapidly adsorb 4-NP and promote the catalytic process. Remarkably, the absorption of 4-NP and reaction kinetics are greatly accelerated when graphitic N or pyrrolic N dopants are introduced to the outer-shell of Fe-N_4 active site [58]. The regulation interaction of peripheral N atoms on the electronic structure of Fe-N_4 was further elucidated by the projected density of state (PDOS) of Fe (Fig. 6d). It can be found that the Fe 3d states of FeN_4+N_G (d_{center} = –0.77 eV) and FeN_4+N_P (d_{center} = –0.82 eV) shifts to higher energy level compared with that of Fe-N_4 (d_{center} = –1.11 eV). Charge density difference analysis further reveals the electron-donating effect of pyrrolic N and graphitic N species on the FeN_4 center (Fig. 6e). Therefore, the peripheral N species, namely N_G or N_P, function as electron donors to restructure the d-band center of FeN_4+N_x (where x = G and P) and modulate the catalytic property. Furthermore, the influence of doping amount of peripheral N species on the catalytic activity was investigated (Figure S14). As shown in Fig. 6f, the d-band center energy increases first and then decreases with the increasing of peripheral graphitic N, which reaches the highest when two graphitic N atoms are intercalated. Whereas the introduction of pyrrolic N causes continuous rise of the d-band center of Fe. According to the d-band center theory, elevated d-band center energy level means enhanced adsorption capacity with the reaction intermediates, which can theoretically reinforce the catalytic activity. With an optimized ratio of graphitic N (N_G-to-N_{Fe}≈2) and more pyrrolic N species surrounding the Fe-N_4 center, Fe-N-C-800 exhibited a prominent catalytic performance compared with other samples. Based on the above results, it can be concluded that appropriate outer-shell graphitic- and pyrrolic-N dopants surrounding the pyridine-type Fe-N_4

center can efficiently tailor the local electronic structure and contribute to upshift of the d-band center, which dramatically promotes the adsorption of reactant and catalytic kinetics for nitroarene reduction, eventually delivering the unprecedented catalytic performance of Fe-N-C-800.

4. Conclusions

In conclusion, we developed a facile g-C_3N_4-assisted template strategy to anchor atomic pyridine-type Fe-N_4 active sites on highly nitrogen-doped carbon nanosheets. The ratio and type of nitrogen species surrounding the Fe-N_4 centers can be modulated by the carbonization temperature. Appropriate peripheral graphitic and pyrrolic N species can tailor the local electronic structure of the Fe-N_4 active centers and contribute to obvious upshift of the d-band center, which efficiently strengthens the adsorption of reaction intermediates on the Fe-N_4 sites and achieves promoted catalytic kinetics of nitroarene reduction. Consequently, the optimized Fe-N-C-800 single-atom catalyst exhibited impressive 4-NP reduction activity (TOF=13.43 min^{-1}), excellent selectivity (>99 %), and low activation energy (19.44 kJ mol^{-1}) at extremely low reductant dosage (12.5 equivalent), which is superior to most reported precious and non-precious metal catalysts. This work provides a guide for the rational regulation of the coordination environment of single-atom M-N-C catalysts, achieving advanced catalysts for nitroarene reduction and beyond.

Declaration of Competing Interest

The authors declare that they have no known competing financial interests or personal relationships that could have appeared to influence the work reported in this paper.

Data availability

The data that has been used is confidential.

Acknowledgments

This work is financially supported by the National Natural Science Foundation of China (No. 22208375, 22138013, U20A20131), China; the National Key R&D Program of China (No. 2019YFA0708700), China; the National Energy-Saving and Low-Carbon Materials Production and Application Demonstration Platform Program (TC220H06N), China; the Shandong Provincial Natural Science Foundation (No. ZR2019QB016, ZR2018ZC1458), China; the financial support from Taishan Scholar Project of Shandong Province of China (No. ts201712020), China; Technological Leading Scholar of 10000 Talent Project (No. W03020508), China.

Appendix A. Supplementary data

Supplementary data to this article can be found online at https://doi.org/10.1016/j.cej.2023.145181.

References

[1] B. Qiao, A. Wang, X. Yang, L.F. Allard, Z. Jiang, Y. Cui, J. Liu, J. Li, T. Zhang, Single-atom catalysis of CO oxidation using Pt_1/FeO_x, Nat. Chem. 3 (8) (2011) 634–641.
[2] X. Cui, W. Li, P. Ryabchuk, K. Junge, M. Beller, Bridging homogeneous and heterogeneous catalysis by heterogeneous single-metal-site catalysts, Nat. Catal. 1 (2018) 385–397.
[3] A. Wang, J. Li, T. Zhang, Heterogeneous single-atom catalysis, Nat. Rev. Chem. 2 (2018) 65–81.
[4] L. Liu, A. Corma, Metal catalysts for heterogeneous catalysis: from single atoms to nanoclusters and nanoparticles, Chem. Rev. 118 (2018) 4981–5079.
[5] M. Macino, A. Barnes, S. Althahban, R. Qu, E. Gibson, D. Morgan, S. Freakley, N. Dimitratos, C. Kiely, X. Gao, A. Beale, D. Bethell, Q. He, M. Sankar, G. Hutchings, Tuning of catalytic sites in Pt/TiO_2 catalysts for the chemoselective hydrogenation of 3-nitrostyrene, Nat. Catal. 2 (2019) 1132.
[6] B. Han, Y. Guo, Y. Huang, W. Xi, J. Xu, J. Luo, H. Qi, Y. Ren, X. Liu, B. Qiao, T. Zhang, Strong metal-support interactions between Pt single atoms and TiO_2, Angew. Chem. Int. Ed. 59 (29) (2020) 11824–11829.
[7] J. Zhang, C. Zheng, M. Zhang, Y. Qiu, Q.i. Xu, W.-C. Cheong, W. Chen, L. Zheng, L. Gu, Z. Hu, D. Wang, Y. Li, Controlling N-doping type in carbon to boost single-atom site Cu catalyzed transfer hydrogenation of quinoline, Nano Res. 13 (11) (2020) 3082–3087.
[8] B.-H. Lee, S. Park, M. Kim, A.K. Sinha, S.C. Lee, E. Jung, W.J. Chang, K.-S. Lee, J. H. Kim, S.-P. Cho, H. Kim, K.T. Nam, T. Hyeon, Reversible and cooperative photoactivation of single-atom Cu/TiO_2 photocatalysts, Nat. Mater. 18 (6) (2019) 620–626.
[9] X. Wu, H. Zhang, S. Zuo, J. Dong, Y. Li, J. Zhang, Y. Han, Engineering the coordination sphere of isolated active sites to explore the intrinsic activity in single-atom catalysts, Nano-Micro Lett. 13 (2021) 136.
[10] Y. Wang, X. Zheng, D. Wang, Design concept for electrocatalysts, Nano Res. 15 (3) (2022) 1730–1752.
[11] Y. Wang, F. Chu, J. Zeng, Q. Wang, T. Naren, Y. Li, Y. Cheng, Y. Lei, F. Wu, Single atom catalysts for fuel cells and rechargeable batteries: principles, advances, and opportunities, ACS Nano 15 (2021) 210–239.
[12] F. Dong, M. Wu, Z. Chen, X. Liu, G. Zhang, J. Qiao, S. Sun, Atomically dispersed transition metal-nitrogen-carbon bifunctional oxygen electrocatalysts for zinc-air batteries: recent advances and future perspectives, Nano-Micro Lett. 14 (2021) 36.
[13] T. Shen, S. Wang, T. Zhao, Y. Hu, D. Wang, Recent advances of single-atom-alloy for energy electrocatalysis, Adv. Energy Mater. 12 (39) (2022) 2201823.
[14] C. Yan, Y.-L. Liu, Q. Zeng, G.-G. Wang, J.-C. Han, 2D nanomaterial supported single-metal atoms for heterogeneous photo/electrocatalysis, Adv. Funct. Mater. 33 (5) (2023) 2210837.
[15] Y. Wang, Y. Zhang, W. Yu, F. Chen, T. Ma, H. Huang, Single-atom catalysts for energy conversion, J. Mater. Chem. A 11 (6) (2023) 2568–2594.
[16] Z. Pu, I.S. Amiinu, R. Cheng, P. Wang, C. Zhang, S. Mu, W. Zhao, F. Su, G. Zhang, S. Liao, S. Sun, Single-atom catalysts for electrochemical hydrogen evolution reaction: recent advances and future perspectives, Nano-Micro Lett. 12 (2020) 21.
[17] L. Zhang, Y. Ren, W. Liu, A. Wang, T. Zhang, Single-atom catalyst: a rising star for green synthesis of fine chemicals, Natl. Sci. Rev. 5 (2018) 653–672.
[18] H. Yan, C. Su, J. He, W. Chen, Single-atom catalysts and their applications in organic chemistry, J. Mater. Chem. A 6 (19) (2018) 8793–8814.
[19] B. Singh, V. Sharma, R.P. Gaikwad, P. Fornasiero, R. Zboril, M.B. Gawande, Single-atom catalysts: a sustainable pathway for the advanced catalytic applications, Small 17 (2021) 2006473.
[20] Y.X. Wang, X.Z. Cui, L.W. Peng, L.L. Li, J.L. Qiao, H.T. Huang, J.L. Shi, Metal-nitrogen-carbon catalysts of specifically coordinated configurations toward typical electrochemical redox reactions, Adv. Mater. 33 (2021) 2100997.
[21] T. Tang, Z. Wang, J. Guan, Optimizing the electrocatalytic selectivity of carbon dioxide reduction reaction by regulating the electronic structure of single-atom M-N-C materials, Adv. Funct. Mater. 32 (2022) 2111504.
[22] Z. Shi, W. Yang, Y. Gu, T. Liao, Z. Sun, Metal-nitrogen-doped carbon materials as highly efficient catalysts: progress and rational design, Adv. Sci. 7 (15) (2020) 2001069.
[23] X. Luo, X. Wei, H. Wang, W. Gu, T. Kaneko, Y. Yoshida, X. Zhao, C. Zhu, Secondary-atom-doping enables robust Fe-N-C single-Atom catalysts with enhanced oxygen reduction reaction, Nano-Micro Lett. 12 (2020) 163.
[24] R. Shen, L. Hao, Y.H. Ng, P. Zhang, A. Arramel, Y. Li, X. Li, Heterogeneous N-coordinated single-atom photocatalysts and electrocatalysts, Chin. J. Catal. 43 (10) (2022) 2453–2483.
[25] Y. Zhao, W.-J. Jiang, J. Zhang, E.C. Lovell, R. Amal, Z. Han, X. Lu, Anchoring sites engineering in single-atom catalysts for highly efficient electrochemical energy conversion reactions, Adv. Mater. 33 (41) (2021) 2102801.
[26] Y. Zhou, G. Chen, Q. Wang, D. Wang, X. Tao, T. Zhang, X. Feng, K. Müllen, Fe-N-C electrocatalysts with densely accessible Fe-N_4 sites for efficient oxygen reduction reaction, Adv. Funct. Mater. 31 (2021) 2102420.
[27] Y. Chen, S. Ji, C. Chen, Q. Peng, D. Wang, Y. Li, Single-atom catalysts: synthetic strategies and electrochemical applications, Joule. 2 (2018) 1242–1264.
[28] G. Zhang, F. Tang, X. Wang, L. Wang, Y.-N. Liu, Atomically dispersed Co–S–N active sites anchored on hierarchically porous carbon for efficient catalytic hydrogenation of nitro compounds, ACS Catal. 12 (10) (2022) 5786–5794.
[29] X. Li, H. Rong, J. Zhang, D. Wang, Y. Li, Modulating the local coordination environment of single-atom catalysts for enhanced catalytic performance, Nano Res. 13 (7) (2020) 1842–1855.
[30] M. Li, S. Chen, Q. Jiang, Q. Chen, X. Wang, Y. Yan, J. Liu, C. Lv, W. Ding, X. Guo, Origin of the activity of Co–N–C catalysts for chemoselective hydrogenation of nitroarenes, ACS Catal. 11 (5) (2021) 3026–3039.
[31] Y. Jia, X. Xiong, D. Wang, X. Duan, K. Sun, Y. Li, L. Zheng, W. Lin, M. Dong, G. Zhang, W. Liu, X. Sun, Atomically dispersed Fe-N_4 modified with precisely located S for highly efficient oxygen reduction, Nano-Micro Lett. 12 (2020) 116.
[32] J.-C. Li, H. Zhong, M. Xu, T. Li, L. Wang, Q. Shi, S. Feng, Z. Lyu, D. Liu, D. Du, S. P. Beckman, X. Pan, Y. Lin, M. Shao, Boosting the activity of Fe-Nx moieties in Fe-N-C electrocatalysts via phosphorus doping for oxygen reduction reaction, Sci. China Mater. 63 (6) (2020) 965–971.
[33] K. Yuan, D. Lutzenkirchen-Hecht, L. Li, L. Shuai, Y. Li, R. Cao, M. Qiu, X. Zhuang, M.K.H. Leung, Y. Chen, U. Scherf, Boosting oxygen reduction of single iron active sites via geometric and electronic engineering: nitrogen and phosphorus dual coordination, J. Am. Chem. Soc. 142 (2020) 2404–2412.

[34] H. Jin, P. Li, P. Cui, J. Shi, W. Zhou, X. Yu, W. Song, C. Cao, Unprecedentedly high activity and selectivity for hydrogenation of nitroarenes with single atomic Co_1-N_3P_1 sites, Nat. Commun. 13 (2022) 723.
[35] Z. Luo, R. Nie, V. Nguyen, A. Biswas, R. Behera, X. Wu, T. Kobayashi, A. Sadow, B. Wang, W. Huang, L. Qi, Transition metal-like carbocatalyst, Nat. Commun. 11 (2020) 4091.
[36] J. Wu, S. Ma, J. Sun, J. Gold, C. Tiwary, B. Kim, L. Zhu, N. Chopra, I. Odeh, R. Vajtai, A. Yu, R. Luo, J. Lou, G. Ding, P. Kenis, P. Ajayan, A metal-free electrocatalyst for carbon dioxide reduction to multi-carbon hydrocarbons and oxygenates, Nat. Commun. 7 (2016) 13869.
[37] F. Yang, C. Chi, C. Wang, Y. Wang, Y. Li, High graphite N content in nitrogen-doped graphene as an efficient metal-free catalyst for reduction of nitroarenes in water, Green Chem. 18 (15) (2016) 4254–4262.
[38] H. Wei, X. Liu, A. Wang, L. Zhang, B. Qiao, X. Yang, Y. Huang, S. Miao, J. Liu, T. Zhang, FeO_x-supported platinum single-atom and pseudo-single-atom catalysts for chemoselective hydrogenation of functionalized nitroarenes, Nat. Commun. 5 (2014) 5634.
[39] W. Liu, H. Feng, Y. Yang, Y. Niu, L. Wang, P. Yin, S. Hong, B. Zhang, X. Zhang, M. Wei, Highly-efficient RuNi single-atom alloy catalysts toward chemoselective hydrogenation of nitroarenes, Nat. Commun. 13 (2022) 3188.
[40] P. Zhou, L. Jiang, F. Wang, K. Deng, K. Lv, Z. Zhang, High performance of a cobalt–nitrogen complex for the reduction and reductive coupling of nitro compounds into amines and their derivatives, Sci. Adv. 3 (2) (2017) e160195.
[41] Y. Song, R. Guo, B. Feng, Y. Fu, F. Zhang, Y. Zhang, D.-L. Chen, J. Zhang, W. Zhu, Coordination number engineering of Zn single-atom sites for enhanced transfer hydrogenation performance, Chem. Eng. J. 465 (2023), 142920.
[42] J. Liu, Y. Zhang, L. Zhang, F. Xie, A. Vasileff, S.Z. Qiao, Graphitic carbon nitride (g-C_3N_4)-derived N-rich graphene with tuneable interlayer distance as a high-rate anode for sodium-ion batteries, Adv. Mater. 31 (2019) e1901261.
[43] S. Han, D. Ma, S. Zhou, K. Zhang, W. Wei, Y. Du, X. Wu, Q. Xu, R. Zou, Q. Zhu, Fluorine-tuned single-atom catalysts with dense surface Ni-N_4 sites on ultrathin carbon nanosheets for efficient CO_2 electroreduction, Appl. Catal. B-Environ. 283 (2021), 119591.
[44] Q. Zhao, W. Ni, X. Tan, F. Cao, T. Liu, H. Huang, Z. Cheng, Y. Li, S. He, H. Ning, M. Wu, A "trojan horse" strategy towards robust Co-N_4 active sites accommodated in micropore defect-rich carbon nanosheets for boosting selective hydrogenation of nitroarenes, J. Mater. Chem. A 10 (17) (2022) 9435–9444.
[45] Y. Chen, Z. Li, Y. Zhu, D. Sun, X. Liu, L. Xu, Y. Tang, Atomic Fe dispersed on N-doped carbon hollow nanospheres for high-efficiency electrocatalytic oxygen reduction, Adv. Mater. 31 (2019) 1806312.
[46] T. Ma, X. Tan, Q. Zhao, Z. Wu, F. Cao, J. Liu, X. Wu, H. Liu, X. Wang, H. Ning, M. Wu, Template-oriented synthesis of Fe–N-codoped graphene nanoshells derived from petroleum pitch for efficient nitroaromatics reduction, Ind. Eng. Chem. Res. 59 (1) (2020) 129–136.
[47] Y. Qiu, L. Fan, M. Wang, X. Yin, X. Wu, X. Sun, D.a. Tian, B. Guan, D. Tang, N. Zhang, Precise synthesis of Fe-N_2 sites with high activity and stability for long-life lithium-sulfur batteries, ACS Nano 14 (11) (2020) 16105–16113.
[48] S. Wu, H. Liu, G. Lei, H. He, J. Wu, G. Zhang, F. Zhang, W. Peng, X. Fan, Y. Li, Single-atomic iron-nitrogen 2D MOF-originated hierarchically porous carbon catalysts for enhanced oxygen reduction reaction, Chem. Eng. J. 441 (2022), 135849.
[49] Y. Chen, S. Ji, Y. Wang, J. Dong, W. Chen, Z. Li, R. Shen, L. Zheng, Z. Zhuang, D. Wang, Y. Li, Isolated single iron atoms anchored on N-doped porous carbon as an efficient electrocatalyst for the oxygen reduction reaction, Angew. Chem. Int. Ed. 56 (24) (2017) 6937–6941.
[50] L. Liu, Y. Duan, Y. Liang, A. Kan, L. Wang, Q. Luo, Y. Zhang, B. Zhang, Z. Li, D. Liu, D. Wang, Cyclized polyacrylonitrile as a promising support for single atom metal catalyst with synergistic active site, Small 18 (2022) 2104142.
[51] C. Nguyen, S. Lee, Y. Chung, W. Chiang, K. Wu, Synergistic effect of metal-organic framework-derived boron and nitrogen heteroatom-doped three-dimensional porous carbons for precious-metal-free catalytic reduction of nitroarenes, Appl. Catal. B-Environ. 257 (2019), 117888.
[52] W. Jiang, L. Gu, L. Li, Y. Zhang, X. Zhang, L. Zhang, J. Wang, J. Hu, Z. Wei, L. Wan, Understanding the high activity of Fe-N-C electrocatalysts in oxygen reduction: Fe/Fe_3C nanoparticles boost the activity of Fe-N_x, J. Am. Chem. Soc. 138 (2016) 3570–3578.
[53] E. Zhang, L. Tao, J. An, J. Zhang, L. Meng, X. Zheng, Y. Wang, N. Li, S. Du, J. Zhang, D. Wang, Y. Li, Engineering the local atomic environments of indium single-atom catalysts for efficient electrochemical production of hydrogen peroxide, Angew. Chem. Int. Ed. 61 (2022) e202117347.
[54] J. Liu, J. Li, P. Jian, R. Jian, I Intriguing hierarchical Co@NC microflowers in situ assembled by nanoneedles: Towards enhanced reduction of nitroaromatic compounds via interfacial synergistic catalysis, J. Hazard. Mater. 403 (2021), 123987.
[55] S. Jiang, L. Wang, Y. Duan, J. An, Q. Luo, Y. Zhang, Y. Tang, J. Huang, B. Zhang, J. Liu, D. Wang, A novel strategy to construct supported silver nanocomposite as an ultra-high efficient catalyst, Appl. Catal. B-Environ. 283 (2021), 119592.
[56] Y. Gu, A. Wu, L. Wang, D. Wang, H. Yan, P. Yu, Y. Xie, C. Tian, F. Sun, H. Fu, A "competitive occupancy" strategy toward Co–N_4 single-atom catalysts embedded in 2D TiN/rGO sheets for highly efficient and stable aromatic nitroreduction, J. Mater. Chem. A 8 (9) (2020) 4807–4815.
[57] Y. Fu, L. Qin, D. Huang, G. Zeng, C. Lai, B. Li, J. He, H. Yi, M. Zhang, M. Cheng, X. Wen, Chitosan functionalized activated coke for Au nanoparticles anchoring: Green synthesis and catalytic activities in hydrogenation of nitrophenols and azo dyes, Appl. Catal. B:-Environ. 255 (2019), 117740.
[58] L. Shi, X. Lin, F. Liu, Y. Long, R. Cheng, C. Tan, L. Yang, C. Hu, S. Zhao, D. Liu, Geometrically deformed iron-based single-atom catalysts for high-performance acidic proton exchange membrane fuel cells, ACS Catal. 12 (9) (2022) 5397–5406.